# Developing a Dust Emission Procedure for Central Asia

Authors: Li, Longlei, and Sokolik, Irina N

Source: Air, Soil and Water Research, 10(1)

Published By: SAGE Publishing

URL: https://doi.org/10.1177/1178622117711939

# Developing a Dust Emission Procedure for Central Asia

Air, Soil and Water Research
Volume 10: 1–12
© The Author(s) 2017
Reprints and permissions:
sagepub.co.uk/journalsPermissions.nav
DOI: 10.1177/1178622117711939

Longlei Li and Irina N Sokolik

School of Earth and Atmospheric Sciences, Georgia Institute of Technology, Atlanta, GA, USA.

**ABSTRACT:** Airborne mineral dust is thought to have a significant influence on the climate through absorbing and scattering both shortwave and longwave radiations and affecting cloud microphysical processes. However, a knowledge of long-term dust emissions is limited from both temporal and spatial perspectives. Here, we have developed a quantitative climatology: the column-integrated mass of the dust aerosol loading in Central Asia by incorporating the dust module (DuMo) into the Weather Research and Forecasting coupled with Chemistry (WRF-Chem) model and accounting for regional climate and Land-Cover and Land-Use Changes for the 1950-2010 period in April. This data set is lowly to moderately correlated (0.22-0.48) with the satellite Aerosol Optical Depth in April of the 2000s and lowly correlated (0.02-0.11) with the Absorbing Aerosol Index in April of the 1980s, 1990s, and 2000s. The total dust loading is approximately 207.85 Mton per month in April during the recent decade (2000-2014) over dust source regions. Although only the month of April was simulated, results suggest that trends and magnitudes are captured well, using the WRF-Chem-DuMo.

**KEYWORDS:** Dust modelling, Central Asia, dust climatology, WRF-Chem, AOD, AAI

**RECEIVED:** January 18, 2017. **ACCEPTED:** May 1, 2017.

**PEER REVIEW:** Seven peer reviewers contributed to the peer review report. Reviewers' reports totalled 3530 words, excluding any confidential comments to the academic editor.

**TYPE:** Original Research

**FUNDING:** The author(s) disclosed receipt of the following financial support for the research, authorship, and/or publication of this article: This work is funded by the NASA LCLUC Program.

**DECLARATION OF CONFLICTING INTERESTS:** The author(s) declared no potential conflicts of interest with respect to the research, authorship, and/or publication of this article.

**CORRESPONDING AUTHOR:** Longlei Li, School of Earth and Atmospheric Sciences, Georgia Institute of Technology, 311 Ferst Drive, Atlanta, GA 30332-0340, USA.
Email: lli353@gatech.edu

## Introduction

The potential effects of mineral aerosols on the Earth's energy balance and hydrological cycle have been recognized since the early 1990s. Dust particles can absorb and scatter shortwave and longwave radiation,[1,2] interact with cloud microphysical processes, influence the snow albedo,[3] and modify precipitation processes.[4,5] However, a large concern is to quantify variability in the dust emission rate in response to the ever-changing global climate system, land-cover, and land-use states, especially in desert landscape regions with lower resistances and high resilience.[6]

Taking advantage of its wide spectral range and strong spectral contrast in response to aerosol properties, the launch of the Moderate Resolution Imaging Spectroradiometer (MODIS) on the Earth Observing System (EOS) satellite makes a consistent, reliable data set for monitoring dust aerosol available.[7] Dust aerosol data sets derived from the MODIS have promoted a series of studies on dust transport[8–11] and dust aerosol properties[12–14] and the aerosol's interaction with clouds[15] and precipitation processes.[16] Based on MODIS aerosol products, several papers have documented the aerosol climatology on a global scale.[17]

However, the current satellite observation for the dust emission is still limited in the time span of the available satellite aerosol products. Besides, current satellite sensors are incapable of accurately quantifying the dust emission due to technique issues such as the cloud contamination. Thus, we turn to a fully coupled regional Weather Research and Forecasting coupled with Chemistry (WRF-Chem)-DuMo model to construct a dust emission in Central Asia. The WRF-Chem model is widely used to simulate trace gases and particulates with the meteorological fields. The DuMo is a dust module that includes 3 dust emission schemes and an integrated system in preprocessing the land surface and dealing with the initial injection issue and the particle size distribution. This climatology data set is expected to serve as a model-data-comparison median with the satellite observation and in situ measurement and as a candidate for a comparison with results from other models or dust schemes.

Furthermore, Central Asia is one of the largest semi-dry regions and is strongly affected by both the warming climate trend[18] and various human activities[19] (eg, massive land and water management projects). In Kazakhstan, the land degradation has begun in the 1950s for the grain production, a shift in an animal (cattle, sheep, and goats) number from 80 million in 1992 down to 44 million in 1999 and up to 63 million in 2005,[18] and changes in grazing practices. Biogenic crusts in the Kara Kum and Kyzyl Kum deserts of Turkmenistan and Uzbekistan have experienced an accelerated growth[18] due to a decrease in the grazing pressure on desert rangelands during the past 40 to 50 years.

Changes in the land surface state can enhance or suppress the dust emission through aeolian roughness and soil moisture dynamics on a daily/seasonally/annually timescale. To our knowledge, there are few published papers which document the dust emission in Central Asia, accounting for Land-Cover and Land-Use Change (LCLUC) and regional climate changes.[20] The main goals of this article are to quantify the dust source strength in Central Asia and to construct a dust emission inventory. To fulfil these goals, we incorporated the DuMo, which is developed by our group,[20,21] into the WRF-Chem and then performed a simulation in April for the period 1950-2015.

## Data Preparation and Model Design

### *Brief description of a physics-based dust scheme in DuMo*

The DuMo system includes 2 different physically based dust emission schemes and 1 simple empirically based scheme. It contains a complex land surface component dealing with surface dynamics, a variation of the surface roughness length and density, for Central Asia. Here, we employed a physics-based scheme, originally developed by Marticorena et al,[22] to calculate the size-dependent dust emission flux $(dF(D))$, which is estimated to be proportional to the size-dependent horizontal flux by an empirical efficiency $\beta$ (equation 1) where $\beta = 16\,300\,\mathrm{cm\,s^{-2}}$. Integrating equation 2 over the total diameter range of soil particles yields the aggregate horizontal flux:

$$dF\left(D\right) = \beta dG\left(D\right) \tag{1}$$

$$dG\left(D\right) = E\frac{\rho_a}{g}U_*^3\left(1+\frac{U_{*_t}}{U_*}\right)\left(1-\frac{U_{*_t}^2}{U_*^2}\right)dS_{rel}\left(D\right)dD \tag{2}$$

Here, $U_*$ denotes the friction velocity; $U_{*_t}$ is the threshold friction velocity at which erosion initiates; $\rho_a$ represents the air density, a prognostic variable in the WRF-Chem-DuMo model; $g$ is the gravitational acceleration parameter; $dS_{rel}(D)$ is the relative surface area covered by a particle of diameter D; and E is a ratio of the erodible to total surface area. We set this ratio to 1, based on an analysis of extensive sets of artificial soil size distributions.[23,24]

The dust emission scheme calculates $U_*$ using a logarithmic wind profile and employing a static aeolian roughness map from the POLDER (POLarization and Directionality of the Earth's Reflectances) instrument data. The threshold friction velocity is calculated by applying a soil moisture correction and a surface roughness correction due to the presence of non-erodible elements such as peddles and rocks to the smooth friction velocity $(U_{*_{ts}})$. The soil moisture correction is only introduced when the soil moisture exceeds the minimal soil moisture (the so-called soil residual moisture) that the soil can hold. The roughness correction is made when the aeolian roughness exceeds a local roughness length of the uncovered smooth surface. Therefore, both corrections are tightly associated with the soil texture and, thus, the land surface state.

### *Input data for the coupled model*

Many global land surface maps, eg, the US Geological Survey (USGS), International Geosphere-Biosphere Program (IGBP) at 1-km spatial resolution,[25] and GLC2000,[26] have been developed using remote sensing imagery from the Advanced Very High Resolution Radiometer (AVHRR) or/and the MODIS. However, currently no land-cover data were available for a regional application (eg, the regional environment modelling). Furthermore, the 24-category USGS data (Figure 1) used in the WRF-Chem model by default cannot represent LCLUC state of periods other than 1992-1993 because it was derived from AVHRR data during the period 1992-1993 only. To better reflect the surface state variation, we modified the default land surface categories in the model based on the Land-Use Harmonization (LUH) data set, literature record, and satellite imagery data.

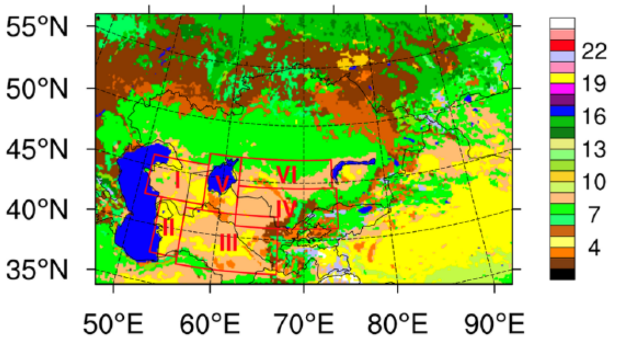

**Figure 1.** The default land-cover and land-use map in the WRF-Chem for Central Asia. The red boxes denote different dust source regions in Central Asia. These regions are located over the Ustyurt Plateau (I), eastern shore of the Caspian Sea (II), Kara Kum desert (III), Kyzyl Kum desert (IV), Aral Kum desert (V), and Muyun Kum desert (VI). Classification of the USGS categories (1-24): 1. urban and built-up land, 2. dryland cropland and pasture, 3. irrigated cropland and pasture, 4. mixed dryland/irrigated cropland and pasture, 5. cropland/grassland mosaic, 6. cropland/woodland mosaic, 7. grassland, 8. shrubland, 9. mixed shrubland/grassland, 10. savanna, 11. deciduous broadleaf, 12. deciduous needleleaf, 13. evergreen broadleaf, 14. evergreen needleleaf, 15. mixed forest, 16. water bodies, 17. herbaceous wetland, 18. wooden wetland, 19. barren or sparsely vegetated, 20. herbaceous tundra, 21. wooded tundra, 22. mixed tundra, 23. bare ground tundra, and 24. snow or ice.

The LUH data set was initially prepared for assessing the effect of the human activity on the carbon-climate system in the Earth System Models. It provides the first set of a consistent land-use change record for the period 1500-2100 at a $0.5° \times 0.5°$ resolution.[27] We modified the USGS categories in the model to reflect the shrinking of the Aral Sea, the back and forth between drying and refilling of the Kara-Bogaz-Gol (KBG) bay, the fluctuation of the Caspian Sea water level, and the Kazakh Steppe. The Aral Sea surface area had shrunk from approximately 67 100 to 7000 km$^2$ by the year 2009, which converts the exposed eastern lakebeds to a new active desert, the Aral Kum. Accordingly, we replaced the original water mask with the land mask #19 (barren or sparsely vegetated category). The KBG bay situates on the eastern coast of the Caspian Sea and extends into the hinterland. A dam built between the Caspian Sea and the bay[28] in March 1980 caused the groundwater level to drop significantly during the 1980s. The nearly dried out bay became a salt flat prone to wind erosion. Correspondingly, for the modelling in the 1980s, we assigned the bay to a 'barren or sparsely vegetated' type (Figure 2: 1980s) but restored the water mask for the 1990s after the bay was refilled in June 1992 (Figure 2: 1990s).

We then reconstructed the cropland and pasture distributions. Arable cropped lands occupied only approximately 8% of the total geographic area. Of those croplands, 36% are fed up with from inland seas or rivers, eg, the Amu Darya and the Syr Darya. The amount of irrigated cropland expanded from 4.5 Ma in 1960 to 7.9 Ma in 2009. Pasture and grass cover most of the lands in Central Asia. In Kyrgyzstan, nearly 90% of the agriculture lands belong to pasture. To reconstruct the cropland

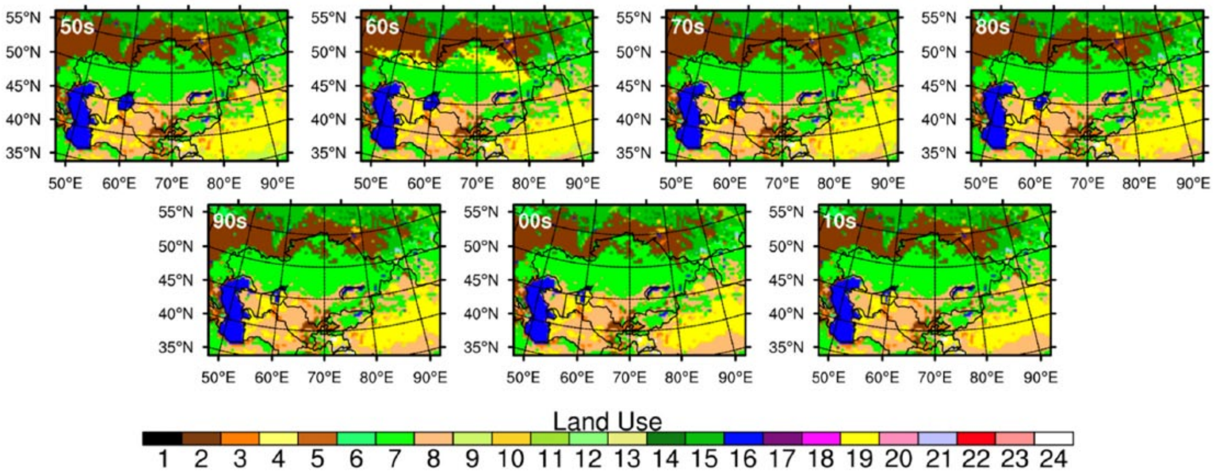

**Figure 2.** Reconstructions of the historical LCLUC in Central Asia during the 1950-2010 decades. Land classification categories are shown in Figure 1.

**Table 1.** Size bin information in the coupled model.

| BIN 1 TO BIN 5 | BIN 6 TO BIN 10 | BIN 11 TO BIN 15 | BIN 16 TO BIN 20 |
|---|---|---|---|
| 0.10–0.22 | 1.44–1.73 | 3.30–3.79 | 7.07–8.41 |
| 0.22–0.46 | 1.73–2.08 | 3.79–4.35 | 8.41–10.00 |
| 0.46–1.00 | 2.08–2.50 | 4.35–5.00 | 10.00–15.18 |
| 1.00–1.20 | 2.50–2.87 | 5.00–5.95 | 15.18–23.05 |
| 1.20–1.44 | 2.87–3.30 | 5.95–7.07 | 23.05–35.00 |

The values represent particle diameters with a unit of micrometre.

and pasture distributions, we split the LUH cropland fractions into 2 components: rainfed and irrigated croplands, corresponding to the category 2 and the category 3 in the default USGS category, respectively. Similarly, we used the LUH pasture fraction to replace the category 7 (grassland) and the category 8 (shrubland) based on their pixel locations. To the north of $45^{\circ}$, we attributed the LUH pasture to the category 7 and category 8 and vice versa.

### *Model configuration*

The WRF-Chem model was configured to cover Central Asia $(50^{\circ}\mathrm{E}-90^{\circ}\mathrm{E}, 37^{\circ}\mathrm{N}-55^{\circ}\mathrm{N})$ with a $10\times10\,\mathrm{km}$ horizontal resolution, centred at $(65^{\circ}\mathrm{E}, 46^{\circ}\mathrm{N})$. To better simulate the near-surface wind velocities, we set 42 vertical layers (10 layers below and 32 layers above 1 km) and set the top layer pressure to $10\,\mathrm{hPa}$.[29] The meteorological fields with lateral boundary and initial conditions took from the National Centers for Environmental Prediction/National Center for Atmospheric Research Reanalysis (R1) data because of its longtime coverage. The chemical lateral boundary condition was provided by the default profile in the WRF-Chem, based on an average of mid-latitude aircraft profiles from several field studies over the Eastern Pacific Ocean.[30] We used a binned method to represent the size distribution in the model, representing the dust particles by 20 bins (Table 1). The climatology data set consists of 2 sub-products, representing fine and coarse dust particles; a sum of column-integrated mass (CIM) from bin 1 to bin 3, CIM for particles in the fine mode (CIM_fine) and a sum of CIM from bin 4 to bin 20, and CIM for particles in the coarse mode (CIM_coarse). Note that CIM is an integration of the mass concentration over the atmosphere column (formula 3):

$$\mathrm{CIM}=\int_{0}^{H} M_c\left(h\right)dh \tag{3}$$

where $M_c(h)$ is the mass concentration with a unit of $\mathrm{g\,m^{-3}}$, $H$ is the height in metre at the top model layer.

A non-parametric test, Mann-Kendall, is used to detect whether a linear trend is present in the CIM time series. The Mann-Kendall test was constructed based on a relative ranking of the data values. It analysed the difference in signs between early and later data points. An increase (decrease) trend presents when the sign values tend to increase (decrease) constantly. This test allowed the existence of autocorrelations among the data values. The Theil-Sen estimation method used here is insensitive to outliers and, thus, it can be significantly more accurate than the simple linear regression.[31] We applied

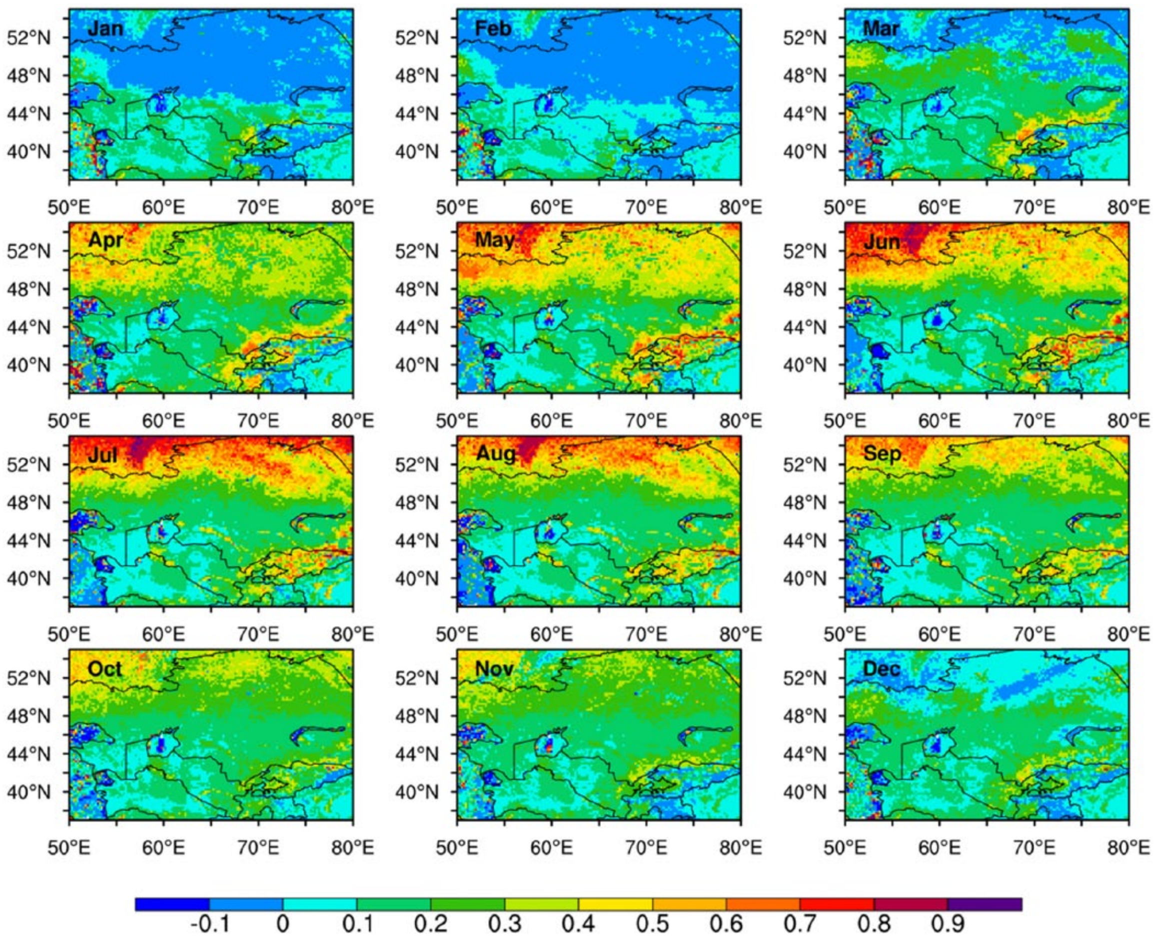

**Figure 3.** Monthly NDVI (MOD13C2) derived from the MODIS/Terra Land Products distributed from the LP DAAC (https://lpdaac.usgs.gov/data_access/data_pool), with a spatial resolution of 0.05° (around 5600 m) for individual months in 2001 over Central Asia.

the trend analysis directly to the CIM series, after proving that there were no annual or seasonal cycles.

Simulations were restricted to April for the 1950-2015 period to demonstrate the 'inter-annual' dust climatology variability and trends owing to the very expensive run time. The month April was selected because of the best match of the land-cover states between the Normalized Difference Vegetation Index (NDVI) (Figure 3) and the LUH data set.

### *Satellite data*

We employed 2 sets of aerosol products, Collection 5.1 (Level 2) and Collection 6 (Level 1) (hereafter referred to as C5 and C6, separately), from the MODIS aboard the Terra to evaluate the modelled dust emission. Aerosol Optical Depth (AOD) is a measure of the ability of scattering and/or absorbing the radiation by aerosols (formula 4). Over a bright desert area, AOD from C5 (Level 2) was retrieved using Deep Blue algorithm (DBA),[32] taking advantage of the smaller surface reflectance in the blue spectral region than in the red and near-infrared channels. The time coverage of the C5 data set (Level 2) is from 2000 to 2007. After 2007, this collection was terminated because of the calibration degradation of the blue channel[33]:

$$\mathrm{AOD} = \int_0^l \alpha(z)\,dz \tag{4}$$

where $l$ is the path length that the light travels and $\alpha(z)$ is the attenuation coefficient.

Recently, Hsu et al[34] further developed an enhanced DBA by combining a surface reflectance database method and a dynamical surface reflectance method based on the NDVI. The NDVI-based reflectance method for vegetated and transitional regions extends the spatial coverage of the retrievals from arid and semiarid regions to the entire land area. In particular, the enhanced DBA added MODIS infrared channels (8.6 and 11 μm) to the aerosol model selection procedure making the retrieval of mineral dust in C6 more accurate than in C5.

Despite those improvements, there are still many missing values over the sub-regions of interest. Therefore, a merged AOD parameter in C6 (a combination of both DBA-based AOD and C6 AOD, referred as C6 hereafter for simplicity) was used instead rather than AOD directly from the enhanced DBA itself. The merged AOD data have fewer spatial gaps and are more continuous during the period 2000-2014. We remapped the best-quality pixels with quality assurance flag 2 or 3

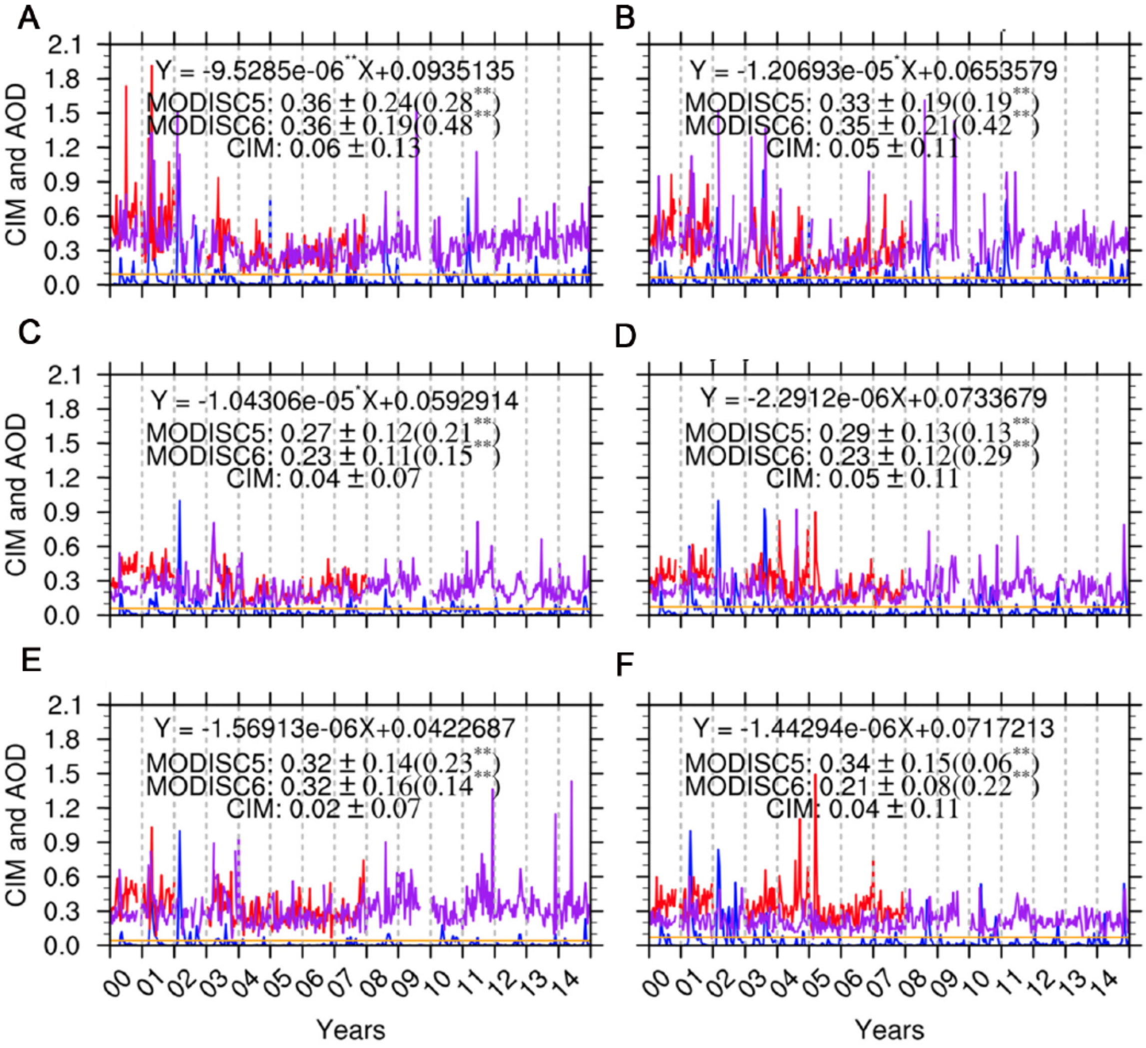

**Figure 4.** Time series of daily averaged C5 (red lines) AOD at 550 nm from 2000 to 2007, merged C6 (purple lines) AOD of MODIS aerosol products from 2000 to 2014, and normalized dust CIM (blue), with units of g m$^{-2}$, at the 6 dust sources in April from 2000 to 2014. The regression line (orange) is also shown. The numbers in each panel show the regression equation for CIM and the monthly mean values ± standard deviations for C5 and C6 AOD and CIM. In addition, the CIM correlation coefficient with C5 and C6 AOD is shown in the parentheses immediately after the standard deviation. The double asterisks (single asterisk) denote that the correlation was significant by Student *t* test at a confidence level of 95% (90%). In this figure, CIM was normalized to a dimensionless variable ranging from 0 to 1. The vertical dashed lines are used to separate months in different years. (A) Ustyurt Plateau, (B) Eastern Shore of the Caspian Sea, (C) Kara Kum desert, (D) Kyzyl Kum desert, (E) Aral Kum desert, and (F) Myun Kum desert. AOD indicates Aerosol Optical Depth; CIM, column-integrated mass; MODIS, Moderate Resolution Imaging Spectroradiometer.

from the original 5-minute 'Swath' granules of both collections into a $0.25° \times 0.25°$ grid and then processed the remapped grid data set into a daily one.

Absorbing Aerosol Index (AAI), derived from sensors on different platform (the Total Ozone Monitoring Satellite [TOMS], Nimbus-7/TOMS, Earth Probe/TOMS, and Aura/Ozone Monitoring Instrument [OMI]), measures to what extent the wavelength dependence of the backward radiation from an atmosphere containing aerosols departures from that of a pure molecular atmosphere in the UV band (formula 5). It is suitable for distinguishing UV-absorbing aerosols,[35] such as dust and biomass burning (larger positive AAI), from weakly absorbing aerosols, the cloud (almost zero AAI), and non-absorbing aerosols (eg, sulphate aerosols and sea-salt particles: negative AAI):

$$\mathrm{AAI} = 100 \log_{10}\left[\frac{I_{360}^{Meas}}{I_{360}^{Calc}}\right] \tag{5}$$

where $I_{360}^{Meas}$ is the measured radiance and $I_{360}^{Calc}$ is the calculated radiance at 360 nm.

## Results and Discussions

### *Comparisons with MODIS AOD*

C5 and C6 AODs are available from 2000 to 2007 and 2000 to 2014, respectively. We performed a comparison between the modelling result and the satellite observation for the 6 desert regions.

Figure 4 shows C5 (red lines) and C6 (purple lines) AOD series for the 6 sub-regions. The mean values shown in the plot

**Table 2.** Mean values of C5 and C6 Aerosol Optical Depth (unitless) and the dust mass per month (unit: Mton) for the 6 dust sources as well as dust mass percentages of the sub-region in the entirety of the 6 desert regions during 2 different periods.

| | 2000–2007 | | | | 2000–2014 | | |
|---|---|---|---|---|---|---|---|
| | C5 | C6 | MASS | CONTRIBUTION (%) | C6 | MASS | CONTRIBUTION (%) |
| I | 0.36 | 0.33 | 30.196 | 12.47 | 0.36 | 26.492 | 12.75 |
| II | 0.33 | 0.33 | 49.319 | 20.36 | 0.35 | 48.249 | 23.21 |
| III | 0.27 | 0.21 | 65.522 | 27.05 | 0.23 | 52.825 | 25.42 |
| IV | 0.29 | 0.20 | 39.239 | 16.20 | 0.23 | 33.715 | 16.22 |
| V | 0.32 | 0.28 | 30.631 | 12.65 | 0.32 | 23.468 | 11.29 |
| VI | 0.34 | 0.21 | 27.298 | 11.27 | 0.21 | 23.101 | 11.11 |

for C5 were for the period 2000-2007. The C6 was averaged during the period 2000-2014, ignoring all missing values in both time series. The Muyun Kum desert is the dustiest region, as indicated by the largest averaged AOD (0.29) in C6. The standard deviation over this sub-region was also the largest (0.15). The newly formed Aral Kum desert has become the second dustiest area with 15-year averaged C6 AOD of 0.22. AOD in C5, however, identified the Ustyurt Plateau (0.36), Muyun Kum (0.34), and the eastern shore of the Caspian Sea (0.33) as the first 3 intensive dust sources. To compare C5 AOD with C6 AOD, we also calculated the C6 AOD mean for the 2000-2007 period. During the calculation, we consider C5 and C6 AOD series in pairs. If either series contained a missing value for a day, we set the data point corresponding to that day in the other series to the missing value too. Results suggested that C5 AOD was higher over the eastern shore of the Caspian Sea, the Kyzyl Kum, and the Aral Kum but smaller over the Muyun Kum and the Ustyurt Plateau (Table 2). Table 2 also gives the absolute relative error for C6 AOD. C5 and C6 AODs have large differences over the Kyzyl Kum (31%), the Kara Kum (22%), and the Muyun Kum (38%) for the period 2000-2007.

Dust CIM is an integration of the dust concentrations over the model vertical layers. We normalized it into 0 and 1 (blue lines in Figure 4) to make a readier comparison with AOD. CIM positively correlates with both C5 and C6 AOD. In particular, the correlations between CIM and C6 AOD over the eastern Caspian Sea and the Ustyurt Plateau reached 0.48 and 0.42, respectively. For all sites on April 9, normalized CIM exceeded the corresponding mean values by at least 1 standard deviation, suggesting that the coupled model successfully reproduced a strong dust event occurred on that day.

All 6 sub-regions show negative trends in the daily CIM series during the 2000-2014 period. However, only the trend over the Ustyurt Plateau was significant at the 95% confidence level. The decreasing trend over the eastern shore of the Caspian Sea and the Kara Kum desert was statistically significant at a confidence level of 90%. The decreasing rate was approximately $-9.53\times10^{-6}\,\mathrm{g\,m^{-2}\,d^{-1}}$ for the Ustyurt Plateau. We analysed the trend in the dust amount using CIM instead of MODIS AOD because randomly distributed missing values in the C5 and C6 time series make the trend estimation from the MODIS difficult.

The contribution (Con) of sub-region $i$ to the total CIM was obtained from formula 6:

$$\mathrm{Con}_i = \frac{\sum_{j=1}^{n_i} \mathrm{CIM}_{ij} \cdot \Delta S_{ij}}{T_{\mathrm{CIM}}} \times 100\% \qquad (6)$$

where $T_{\mathrm{CIM}}$ is the total CIM, $j$ denotes each pixel of the $i$th sub-regions in the model output files, $n_i$ is the pixel number of the $i$th sub-region in the simulation data, $\mathrm{CIM}_i$ represents the CIM for an individual pixel, and $\Delta S_{ij}$ is the area of each pixel. We calculated $\Delta S_{ij}$ using formula 7:

$$\Delta S_{ij} = dx_{ij} \cdot dy_{ij} \qquad (7)$$

where $dx_{ij}$ and $dy_{ij}$ are the ground projection distances of each pixel along the longitude and latitude, respectively.

Total dust CIM was obtained from formula 8:

$$T_{\mathrm{CIM}} = \sum_{i=1}^{m} \sum_{j=1}^{n_i} \mathrm{CIM}_{ij} \cdot \Delta S_{ij} \qquad (8)$$

where $m$ denotes the sub-region number and $n_i$ is the pixel number of the $i$th sub-region.

Table 2 shows the contributions of the sub-averaged to domain-integrated CIM and AOD (C5 and C6). The Kara Kum is the largest contributor to dust CIM in Central Asia, with contributions of 27.05% and 25.42% during the 2000-2007 and 2000-2014 periods, respectively. The eastern shore of the Caspian Sea was another strong dust source only second to the Kara Kum. In contract, the Muyun Kum region was the weakest source with its contribution of only 11.27% and 11.11% for the 2000-2007 and 2000-2014 periods, respectively. From formula 8, dust CIM in the 6 dust regions was estimated to be 242.2 Mton per month in April during the 2000-2007 period and 207.9 Mton per month for the

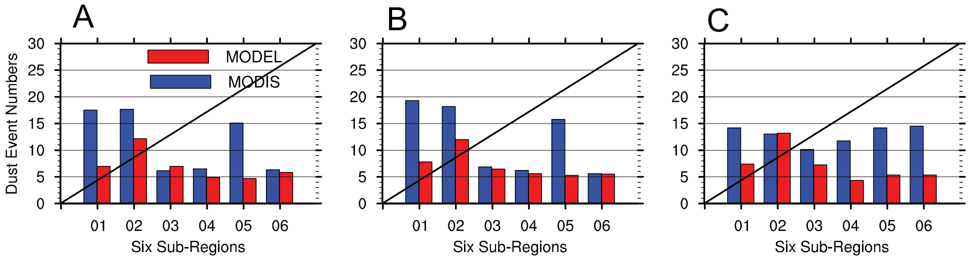

**Figure 5.** The dust event numbers detected by MODIS aerosol products and simulations over the 6 sub-regions. (A) C6 and CIM: 2000-2007, (B) C6 and CIM: 2000–2014, and (C) C5 and CIM: 2000–2007. CIM indicates column-integrated mass; MODIS, Moderate Resolution Imaging Spectroradiometer.

**Table 3.** Threshold values used for detecting dust events during the 2000-2007 and 2000-2014 periods.

| PERIOD | C5 AOD/CIM ($G\,m^{-2}$) | C6 AOD/CIM ($G\,m^{-2}$) |
|---|---|---|
| 2000–2007 | 0.32/0.15 | 0.26/0.16 |
| 2000-2014 | — | 0.28/0.15 |

Abbreviations: AOD, Aerosol Optical Depth; CIM, column-integrated mass.

2000-2014 period. The atmosphere over the dustiest region, the Kara Kum, contained 65.5 Mton (averaged value) and 52.8 Mton dust CIM for the period 2000-2007 and 2000-2014, respectively.

Figure 5 shows the dust event numbers, calculated using CIM and MODIS AOD. We take averaged AOD and CIM for all 6 regions as our threshold value, as shown in Table 3, to detect a dust event. Because the missing values in C5 and C6 AOD do not appear in the same days, the threshold of CIM differs slightly during the 2000-2007 period, making a slight difference in the dust event numbers detected by CIM. Dust event numbers from C6 AOD are very different among the 6 sub-regions, identifying the Ustyurt Plateau, the eastern shore of the Caspian Sea, and the Aral Kum as very active dust sources during the 2 periods. Of these regions, the latter 2 belong to dry unconsolidated lakes, demonstrating the geomorphological signature of MODIS-defined dust sources.[36] In contrast, C5 AOD shows more evenly distributed and less frequent dust events over these sub-regions. Over the Muyun Kum, these 2 collections have the largest discrepancy (Figure 4 and Table 2).

Over the Kara Kum, the Kyzyl Kum, and the Muyun Kum, the dust event numbers from our simulation are comparable with those from C6 AOD. Over the Ustyurt Plateau and the Aral Kum, however, our model significantly underestimates the dust event number. The most frequent dust event from our simulation occurs on the eastern shore of the Caspian Sea with a frequency approximately of 0.4 during both periods. The dust event number from the model in this region is comparable with that from C5 AOD but underestimated by 0.2 (~6 days) in comparison with that from C6 AOD. The evident underestimation of our simulation over the Ustyurt Plateau and the Aral Kum most probably resides in an imperfect dealing with the soil properties, which in turn reflects the importance of including the surface dynamics in dust emission schemes.

### *Comparison with AAI and CIM at the daily scale*

The TOMS sensors, operated for a much longer time than the MODIS does, can provide a rough estimation of the model results before the year 2000. We compared the dust events detected using CIM with those using AAI averaged over all the sub-regions rather than performing a site-to-site comparison (Supplementary Figure 1) because of the low spatial resolution of the AAI data. We separated CIM into 3 periods (1981-1993, 1997-2005, and 2005-2015) to form pairs with AAI from different platforms (corresponding to Nimbus-7/TOMS, Earth Probe/TOMS, and Aura/OMI, respectively). The data are displayed for April only to be consistent with the modelled date.

AAI has the relative variability (defined as the ratio of the standard deviation to the time-series mean) almost 86% less than that of modelled CIM for all the 3 periods. The following factors partially explain the large discrepancy between the relative variability of AAI, 23.0%, 21.9%, and 19.4% and that of CIM, 141.7%, 170.0%, and 138.5% (Supplementary Figure 1) for the 3 periods (1981-1993, 1997-2005, and 2005-2015). First, the averaging of the modelled CIM was over a larger number of grid points than that of MODIS AOD over the sub-regions. Second, AAI contained aerosol information not only for mineral particles but also for smoke and other UV-absorbing anthropogenic aerosols. Third, very small values (less than 0.5[37]) were removed from the AAI data to retain precise retrievals. Finally, AAI reflects the absorbing aerosol loading only at the overpass time. In contrast, averaged CIM from the hourly model output files may contain extremely strong episodes which are not captured by AAI. The large discrepancy in the relative variability also presents between CIM and MODIS AOD (Figure 4). In fact, AAI in the Central Asia poorly correlated with MODIS AOD during 2000-2014 periods (not shown). Very limited amount of AERONET (Aerosol Robotic Network) stations in this region makes an inter-comparison among different satellite retrievals difficult because satellite retrievals require validations by the ground-based observation.

In April, averaged AAI was slightly larger during the period 1997-2005 (1.05) and 2005-2015 (1.08) than during the period 1981-1993 (0.87). We used constant threshold AAI, 1.0, the same as Prospero et al[35] used over the North Atlantic Ocean and Africa, to detect dust events. During the 3 periods, we applied the same threshold CIM to the dust event detection because the model is consistent. The dust event number beginning from 1981 is shown in Figure 6 where very frequent dust events registered in April of 2000 (25 days/month by the Earth Probe/TOMS), 2001 (26 days/month by the Earth Probe/TOMS), 2008 (24 days/month by the by the Aura/OMI), and 2011 (24 days/month by the by the Aura/OMI). In contrast, the model underestimates the event frequency for the recent decade and overestimates it for the decade before 1990.

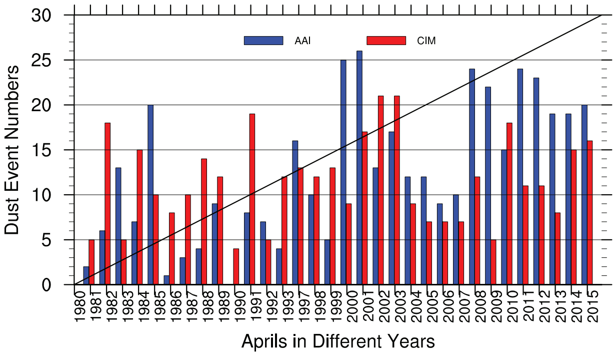

**Figure 6.** Dust event numbers, detected using CIM (red bars) and AAI (blue bars) over all 6 sub-regions for the 1981-2015 period. AAI indicates Absorbing Aerosol Index; CIM, column-integrated mass.

### *The dust emission and a contribution estimation of each source region in April*

To our knowledge, this is the first time anyone has attempted to use a regional coupled model to investigate 'inter-annual' dust variability in Central Asia (although this study was limited to a single month). Figure 7 shows the mean CIM map for CIM_fine, CIM_coarse, and their sum over the entire period 1950-2015. Column-integrated mass for particles in the coarse mode, which dominates long-term averaged CIM because of the larger particle size, had 2 separate high centres. One centre with a higher dust loading appeared on the eastern shore of the

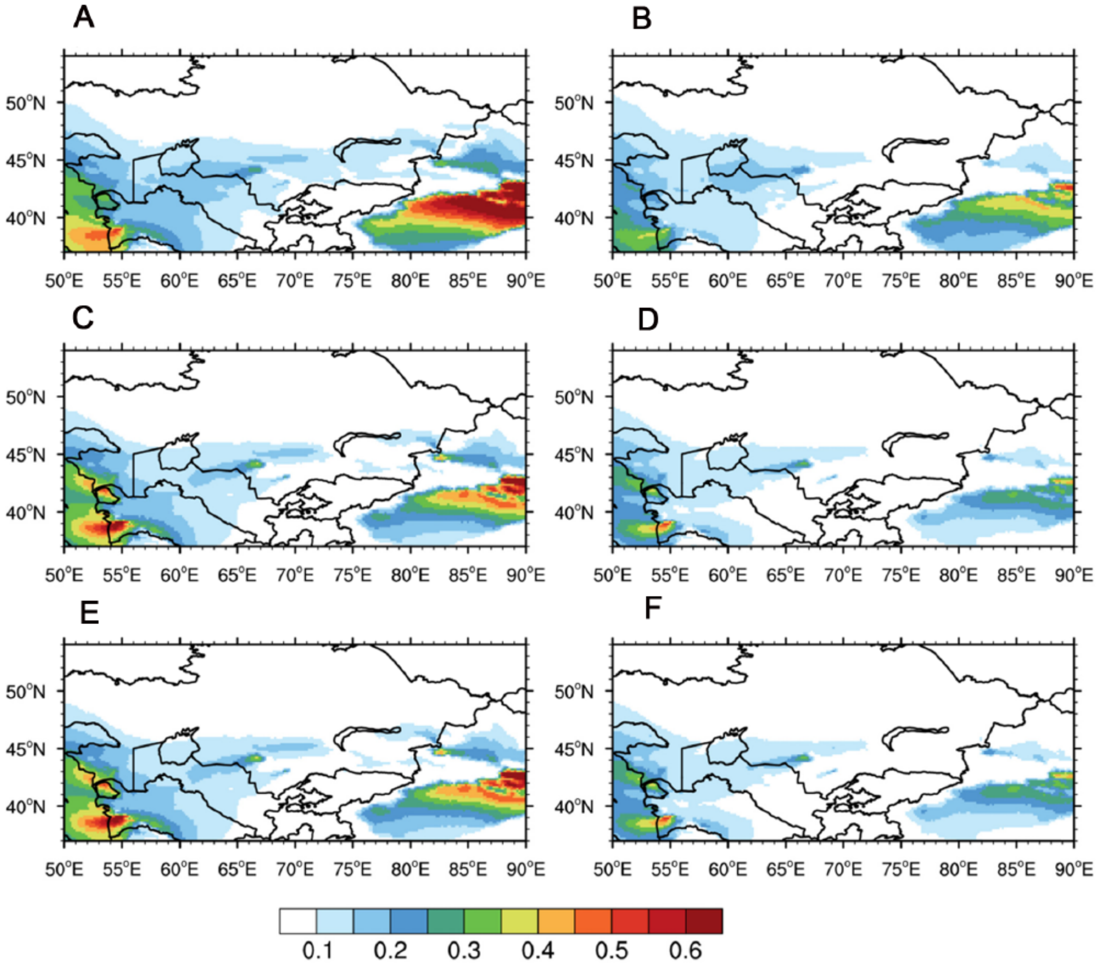

**Figure 7.** Averaged CIM (A for CIM_fine, C for CIM_coarse, and E for their sum) for 1950–2015 period and their standard deviation (B, D, and F for CIM_fine, CIM_coarse, and their sum, respectively). Note that values for fine-mode panels (A and B) have been divided by 100.

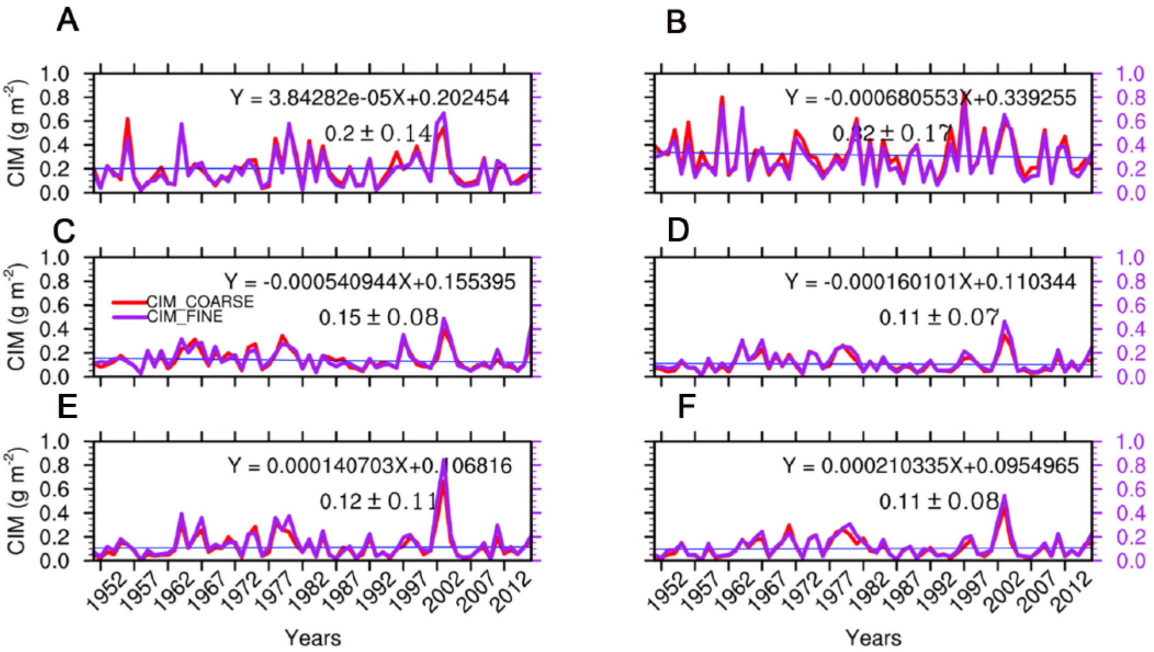

**Figure 8.** The long-term inter-annual variability of CIM (red: CIM_coarse, left *y*-axis; purple: CIM_fine, right *y*-axis) in April for the period 1950-2015 for the 6 sub-regions. The CIM units here are g m$^{-2}$. Note that all values for CIM-fine should be multiplied by $10^2$. (A) Ustyurt Plateau, (B) Eastern Shore of the Caspian Sea, (C) Kara Kum desert, (D) Kyzyl Kum desert, (E) Aral Kum desert, and (F) Myun Kum desert. CIM indicates column-integrated mass.

Caspian Sea (Figure 7). The other centre located near the boundary of the Ustyurt Plateau and the eastern shore of the Caspian Sea. Fine-mode CIM had only 1 centre on the eastern shore of the Caspian Sea. Ranging from 0.1 to 0.3, CIM over the dust belt decreased both northward and southward away from the belt. The distribution of the CIM variability was very similar to that of CIM, where regions with larger dust CIM tend to have larger variability.

Figure 8 shows the inter-annual variability for the 6 sub-regions. The inter-annual variability was very large in April during the past 66 years. Comparisons among different sub-regions show that the active dust 'hot spot' continued locating on the Ustyurt Plateau and the eastern shore of the Caspian Sea. The amount of the dust aerosol in Central Asia had significantly decreased by the end of the 1980s but rapidly increased in 2001. Extremely large CIM appeared in 1979, 1995, and 2001.

In Central Asia, the major dynamic driving forces for the dust lifting and transport result from cyclonic activities and a seasonal shift of the polar front in century timescale.[38] Cyclonic storms can cause severe dust storms when arid conditions prevail, which may explain large CIM in the year of 1979. All causes – meteorological conditions and LCLUC states – must work together to produce mineral dust. As a result of the rapid retreat of the Aral Sea from 1989 to 2009,[39,40] CIM almost exceeded 0.65 in 2001 when the largest CIM registered during the simulation period. However, CIM over that source region remained small in previous 2 decades, until 2001, which is consistent with a previous study.[40]

Figure 9 shows the contribution of each sub-region (averaged over 10 adjacent April months, eg, 10 April months from 1950 to 1959) in dust CIM. The approaches used here illustrate the decade wide variability seen in region dust predictions. In the 1950s, approximately 166.4 Mton of dust particles entered into the atmosphere per month. This value increased to 242.4 Mton in the 1960s and continued increasing to 270.9 Mton in the 1970s. Subsequently, the dust amount in this region dropped greatly to 186.2 and 191.6 Mton in the 1980s and 1990s, respectively. In the 2000s, the total dust amount was estimated to be 224.2 Mton, indicating that Central Asia became very active again. The Caspian Sea, the Kara Kum, and the Kyzyl Kum contributed most of the dust aerosols, comprising nearly 72% of the total dust production in Central Asia.

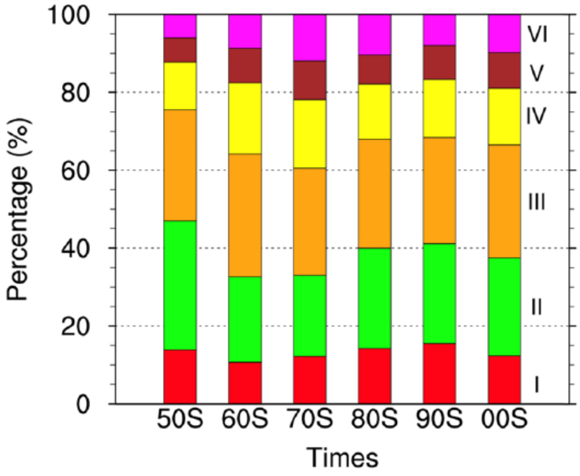

**Figure 9.** 10-April averaged contributions of each sub-region to total column-integrated mass over all the dust source regions with values shown as a percentage (%). For each 100% column, the bottom to the top small columns are for sub-regions I, II, III, IV, V, and VI, respectively.

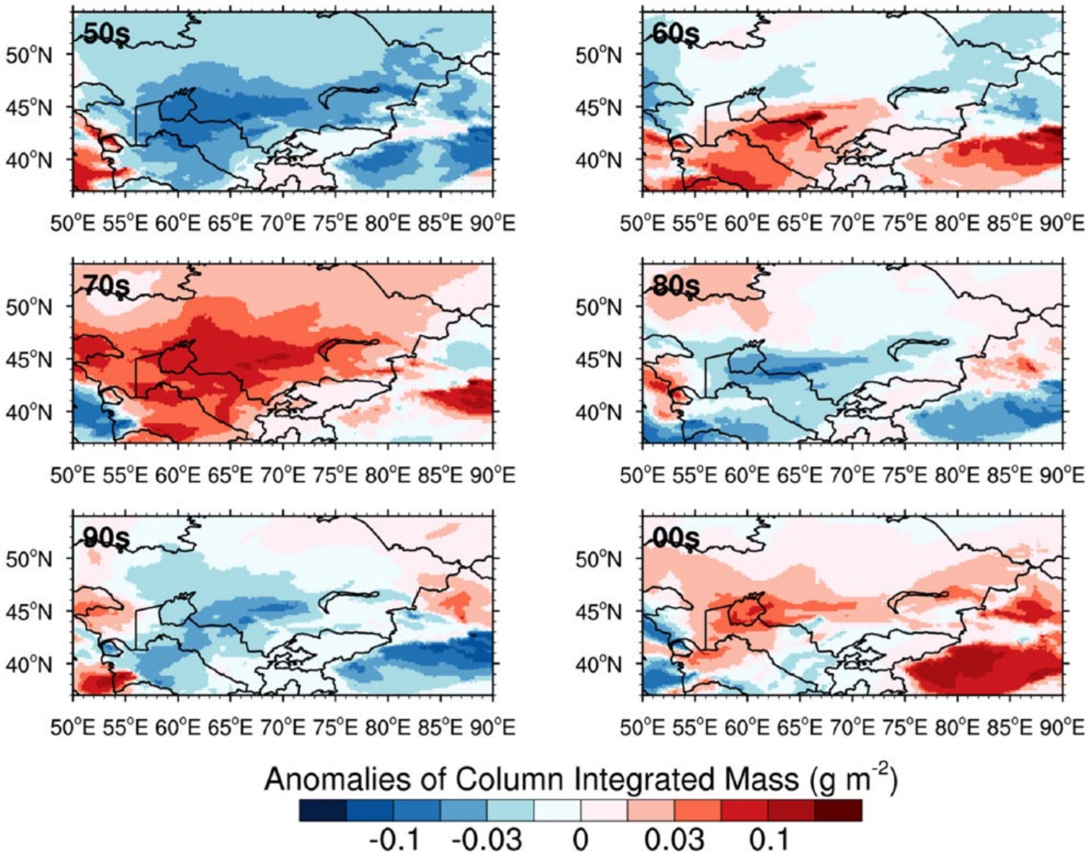

**Figure 10.** 10-month averaged dust CIM anomalies with respect to a 1950-2015 baseline, as shown in Figure 7E.

### *Dust emission anomalies from the model*

We selected long-term (1950-2015) averaged CIM in April as a baseline to calculate the dust anomaly. Figure 10 shows the dust anomaly for different times, eg, the 1980s and the 1990s.

Most water flowing through rivers of the Kara Kum, the Kyzyl Kum, and the Muyun Kum was redirected along canals for various agricultural uses during the 1970s. Resulting from the development of the agricultural irrigation, the desertification process (the desiccation of the Aral Sea, drop of the groundwater level, and an increase in water salinity) got accelerated. This human-related land surface change along with the regional warming[18] and the precipitation decrease, corresponding to strong La Nina events in 1973-1974 and 1975-1976,[41] induced a severe and continuous aridity.[42] The lasting aridity led to a significantly enhanced dust storm frequency[43] and CIM, with the anomaly centre near the Amu Darya and the Syr Darya Rivers (Figure 10: 1970s).

In comparison with previous decades, CIM in the 1980s and 1990s showed a marked decrease (Figures 8 and 10). In those 2 decades, negative anomalies exist over most of Central Asia, especially over the western Turkmenistan and regions between the Aral Sea and the Balkhash Lake. The major 'hot spots' were mainly found at the KBG bay and in the southwestern Turkmenistan in the 1980s and 1990s, respectively, which coincides with an another study.[44]

In the 2000s, positive CIM anomalies appeared over the dust belt, particularly over the Aral Sea and nearby regions, which is consistent with Indoitu et al[45] who reported a doubled increase in dust storm events over the Aral Sea.

Over the KBG, our simulation successfully reproduced enhanced CIM (positive anomalies) in the 1980s. The lower water level of the KBG makes this region more prone to the wind erosion. In fact, the KBG became well known as one of the largest and saltiest bodies of water producing 'Salt storms' during the period 1980-1983.[46] After the dam vanished in the 1990s, this exposed bay refilled by inflows, which efficiently protect the soil from being prone to the dust emission. Accordingly, CIM returned to its lower value during this period. The fluctuation in the CIM anomalies in response to the groundwater-level fluctuation illustrates that the human activity can influence the dust emission intensity through modifying land surface states.

## Summary

We constructed a dust CIM data set for April during the 1950-2015 period by incorporating a dust module, DuMo, into WRF-Chem and modifying the default LCLUC to more realistically represent the land surface state. A comparison between the model result and MODIS C5 and C6 AOD was made for the 6 sub-regions at a daily timescale for the years 2000 to 2007 and 2000 to 2014, respectively. The correlation between CIM and C6 AOD ranges from low to moderate level (0.22-0.48), except for the Kara Kum (0.15) and the Aral Kum (0.14) desert regions, where low correlations are found. In comparison with the correlation with C6 AOD, CIM has a higher correlation with C5 AOD over the Kara Kum and Aral Kum deserts but had a smaller correlation over other sub-regions. The model well reproduced the dust frequency over the Kara Kum, but it underestimates the frequency over the Ustyurt Plateau, the Aral Kum, the eastern shore of the Caspian Sea, and the Aral Sea. The dust frequency derived from CIM is less than that from AAI in April during near recent decades but is more before 1990. In addition, the coupled model generated a very high dust variability on a daily scale, which is almost in the same order of the dust.

Simulation results also suggest that the following: (1) the total dust loading over all 6 desert regions was 207.9 Mton per month for the 2000-2014 period; (2) the Kara Kum (52.8 Mton), the eastern shore of the Caspian Sea (48.2 Mton), and the Muyun Kum (33.7 Mton) were the first 3 large CIM regions during the considering period; and (3) positive anomalies presented in the 1970s (with a larger spatial extension), 1960s, and 2000s.

## Acknowledgements

The cropland and pasture land-use fraction data are available at http://luh.umd.edu/, the MODIS AOD C5/C6 was obtained from the Atmosphere Archive and Distribution System (http://ladsweb.nascom.nasa.gov), and AAI was obtained from the Goddard Earth Sciences Data and Information Services Center (http://disc.sci.gsfc.nasa.gov/data-holdings/). NCEP/NCAR reanalysis data can be found at http://rda.ucar.edu/.

## Author Contributions

LL and INS conceived and designed the experiments, agree with manuscript results and conclusions, jointly developed the structure and arguments for the paper, and made critical revisions and approved final version. LL analysed the data and wrote the first draft of the manuscript. INS contributed to the writing of the manuscript. All authors reviewed and approved the final manuscript.

## Disclosures and Ethics

As a requirement of publication, author(s) have provided to the publisher signed confirmation of compliance with legal and ethical obligations including but not limited to the following: authorship and contributorship, conflicts of interest, privacy and confidentiality, and (where applicable) protection of human and animal research subjects. The authors have read and confirmed their agreement with the ICMJE authorship and conflict of interest criteria. The authors have also confirmed that this article is unique and not under consideration or published in any other publication, and that they have permission from rights holders to reproduce any copyrighted material. Any disclosures are made in this section. The external blind peer reviewers report no conflicts of interest.

## REFERENCES

1. Tegen I, Fung I. Modeling of mineral dust in the atmosphere: sources, transport, and optical-thickness. *J Geophys Res-Atmos*. 1994;99:22897–22914.
2. Sokolik IN, Toon OB. Direct radiative forcing by anthropogenic airborne mineral aerosols. *Nature*. 1996;381:681–683.
3. Painter TH, Barrett AP, Landry CC, et al. Impact of disturbed desert soils on duration of mountain snow cover. *Geophys Res Lett*. 2007;34:1–6.
4. Kluser L, Holzer-Popp T. Relationships between mineral dust and cloud properties in the West African Sahel. *Atmos Chem Phys*. 2010;10:6901–6915.
5. Creamean JM, Suski KJ, Rosenfeld D, et al. Dust and biological aerosols from the Sahara and Asia influence precipitation in the Western U.S. *Science*. 2013;339:1572–1578.
6. Kariyeva J, Van Leeuwen W. Environmental drivers of NDVI-based vegetation phenology in Central Asia. *Remote Sens*. 2011;3:203–246.
7. Kaufman YJ, Tanre D, Remer LA, Vermote EF, Chu A, Holben BN. Operational remote sensing of tropospheric aerosol over land from EOS moderate resolution imaging spectroradiometer. *J Geophys Res-Atmos*. 1997;102:17051–17067.
8. DeMott PJ, Sassen K, Poellot MR, et al. African dust aerosols as atmospheric ice nuclei. *Geophys Res Lett*. 2003;30:1–4.
9. Levy RC, Remer LA, Tanre D, et al. Evaluation of the Moderate-Resolution Imaging Spectroradiometer (MODIS) retrievals of dust aerosol over the ocean during PRIDE. *J Geophys Res-Atmos*. 2003;108:1–13.
10. Kaufman YJ, Koren I, Remer LA, Tanre D, Ginoux P, Fan S. Dust transport and deposition observed from the Terra-Moderate Resolution Imaging Spectroradiometer (MODIS) spacecraft over the Atlantic Ocean. *J Geophys Res-Atmos*. 2005;110:1–16.
11. Engelstaedter S, Tegen I, Washington R. North African dust emissions and transport. *Earth-Sci Rev*. 2006;79:73–100.
12. Tanre D, Kaufman YJ, Herman M, Mattoo S. Remote sensing of aerosol properties over oceans using the MODIS/EOS spectral radiances. *J Geophys Res-Atmos*. 1997;102:16971–16988.
13. Darmenov A, Sokolik IN. Identifying the regional thermal-IR radiative signature of mineral dust with MODIS. *Geophys Res Lett*. 2005;32.
14. Prasad AK, Singh RP. Changes in aerosol parameters during major dust storm events (2001-2005) over the Indo-Gangetic Plains using AERONET and MODIS data. *J Geophys Res-Atmos*. 2007;112:1–8.
15. Brennan JI, Kaufman YJ, Koren I, Li RR. Aerosol-cloud interaction-misclassification of MODIS clouds in heavy aerosol. *IEEE T Geosci Remote*. 2005;43:911–915.
16. Min Q-L, Li R, Lin B, et al. Evidence of mineral dust altering cloud microphysics and precipitation. *Atmos Chem Phys*. 2009;9:3223–3231.
17. Remer LA, Kleidman RG, Levy RC, et al. Global aerosol climatology from the MODIS satellite sensors. *J Geophys Res-Atmos*. 2008;113:1–18.
18. Lioubimtseva E, Henebry GM. Climate and environmental change in arid Central Asia: impacts, vulnerability, and adaptations. *J Arid Environ*. 2009;73:963–977.
19. Lioubimtseva E, Cole R, Adams JM, Kapustin G. Impacts of climate and land-cover changes in arid lands of Central Asia. *J Arid Environ*. 2005;62:285–308.
20. Xi X, Sokolik IN. Seasonal dynamics of threshold friction velocity and dust emission in Central Asia. *J Geophys Res-Atmos*. 2015;120:1536–1564.
21. Darmenova K, Sokolik IN, Darmenov A. Characterization of East Asian dust outbreaks in the spring of 2001 using ground-based and satellite data. *J Geophys Res-Atmos*. 2005;110:1–18.
22. Marticorena B, Bergamett G. Modeling the atmospheric dust cycle: 1. Design of a soil-derived dust emission scheme. *J Geophys Res-Atmos*. 1995;100:16415–16430.
23. Marticorena B, Bergamett G, Gillette D, Belnap J. Factors controlling threshold friction velocity in semiarid and arid areas of the United States. *J Geophys Res-Atmos*. 1997;102:23277–23287.
24. Laurent B, Marticorena B, Bergametti G, Mei F. Modeling mineral dust emissions from Chinese and Mongolian deserts. *Global Planet Change*. 2006;52:121–141.
25. Friedl MA, McIver DK, Hodges JCF, et al. Global land cover mapping from MODIS: algorithms and early results. *Remote Sens Environ*. 2002;83:287–302.
26. Bartholomé E, Belward AS. GLC2000: a new approach to global land cover mapping from Earth observation data. *Int J Remote Sens*. 2005;26:1959–1977.
27. Hurtt GC, Chini LP, Frolking S, et al. Harmonization of land-use scenarios for the period 1500-2100: 600 years of global gridded annual land-use transitions, wood harvest, and resulting secondary lands. *Climatic Change*. 2011;109:117–161.
28. Giralt S, Julia R, Leroy S, Gasse F. Cyclic water level oscillations of the KaraBogazGol-Caspian Sea system. *Earth Planet Sc Lett*. 2003;212:225–239.
29. Todd MC, Bou Karam D, Cavazos C, et al. Quantifying uncertainty in estimates of mineral dust flux: an intercomparison of model performance over the Bodélé Depression, northern Chad. *J Geophys Res-Atmos*. 2008;113:1–22.

30. Zhao C, Liu X, Leung LR, et al. The spatial distribution of mineral dust and its shortwave radiative forcing over North Africa: modeling sensitivities to dust emissions and aerosol size treatments. *Atmos Chem Phys*. 2010;10:8821–8838.
31. Wilcox RR. *Fundamentals of Modern Statistical Methods: Substantially Improving Power and Accuracy*. Berlin, Germany: Springer; 2001:207–210.
32. Hsu NC, Tsay S-C, King MD. Aerosol properties over bright-reflecting source regions. *IEEE T Geosci Remote*. 2004;42:557–569.
33. Lyapustin A, Wang Y, Xiong X, et al. Scientific impact of MODIS C5 calibration degradation and C6+ improvements. *Atmos Meas Tech*. 2014;7:4353–4365.
34. Hsu NC, Jeong MJ, Bettenhausen C, et al. Enhanced Deep Blue aerosol retrieval algorithm: the second generation. *J Geophys Res-Atmos*. 2013;118:9296–9315.
35. Prospero JM, Ginoux P, Torres O, Nicholson SE, Gill TE. Environmental characterization of global sources of atmospheric soil dust identified with the NIMBUS 7 Total Ozone Mapping Spectrometer (TOMS) absorbing aerosol product. *Rev Geophys*. 2002;40:2-1-2-31.
36. Baddock MC, Ginoux P, Bullard JE, Gill TE. Do MODIS-defined dust sources have a geomorphological signature? *Geophys Res Lett*. 2016;43:2606–2613.
37. Chiapello I, Prospero JM, Herman JR, Hsu NC. Detection of mineral dust over the North Atlantic Ocean and Africa with the Nimbus 7 TOMS. *J Geophys Res-Atmos*. 1999;104:9277–9291.
38. Machalett B, Oches EA, Frechen M, et al. Aeolian dust dynamics in central Asia during the Pleistocene: driven by the long-term migration, seasonality, and permanency of the Asiatic polar front. *Geochem Geophy Geosy*. 2008;9:1–22.
39. Kozhoridze G, Orlovsky L, Orlovsky N. Monitoring land cover dynamics in the Aral Sea region by remote sensing. *Proc SPIE*. 2012;8538:85381V.
40. Indoitu R, Kozhoridze G, Batyrbaeva M, et al. Dust emission and environmental changes in the dried bottom of the Aral Sea. *Aeolian Res*. 2015;17:101–115.
41. Barlow M, Cullen H, Lyon B. Drought in central and southwest Asia: La Niña, the warm pool, and Indian Ocean precipitation. *J Climate*. 2002;15:697–700.
42. Saiko TA, Zonn IS. Irrigation expansion and dynamics of desertification in the Circum-Aral region of Central Asia. *Appl Geogr*. 2000;20:349–367.
43. Littmann T. Dust storm frequency in Asia: climatic control and variability. *Int J Climatol*. 1991;11:393–412.
44. Orlovsky L, Orlovsky N, Durdyev A. Dust storms in Turkmenistan. *J Arid Environ*. 2005;60:83–97.
45. Indoitu R, Orlovsky L, Orlovsky N. Dust storms in Central Asia: spatial and temporal variations. *J Arid Environ*. 2012;85:62–70.
46. Gill TE. Eolian sediments generated by anthropogenic disturbance of playas: human impacts on the geomorphic system and geomorphic impacts on the human system. *Geomorphology*. 1996;17:207–228.